NASA Technical Memorandum 4371

Structural Characterization of a First-Generation Articulated-Truss Joint for Space Crane Application

Thomas R. Sutter, K. Chauncey Wu,
Kevin T. Riutort, Joseph B. Laufer,
and James E. Phelps

MAY 1992

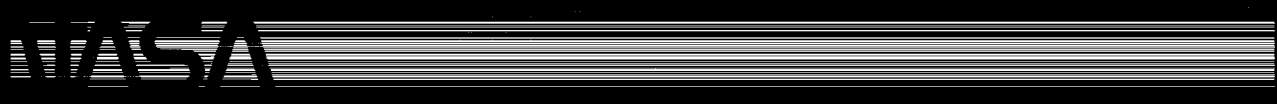

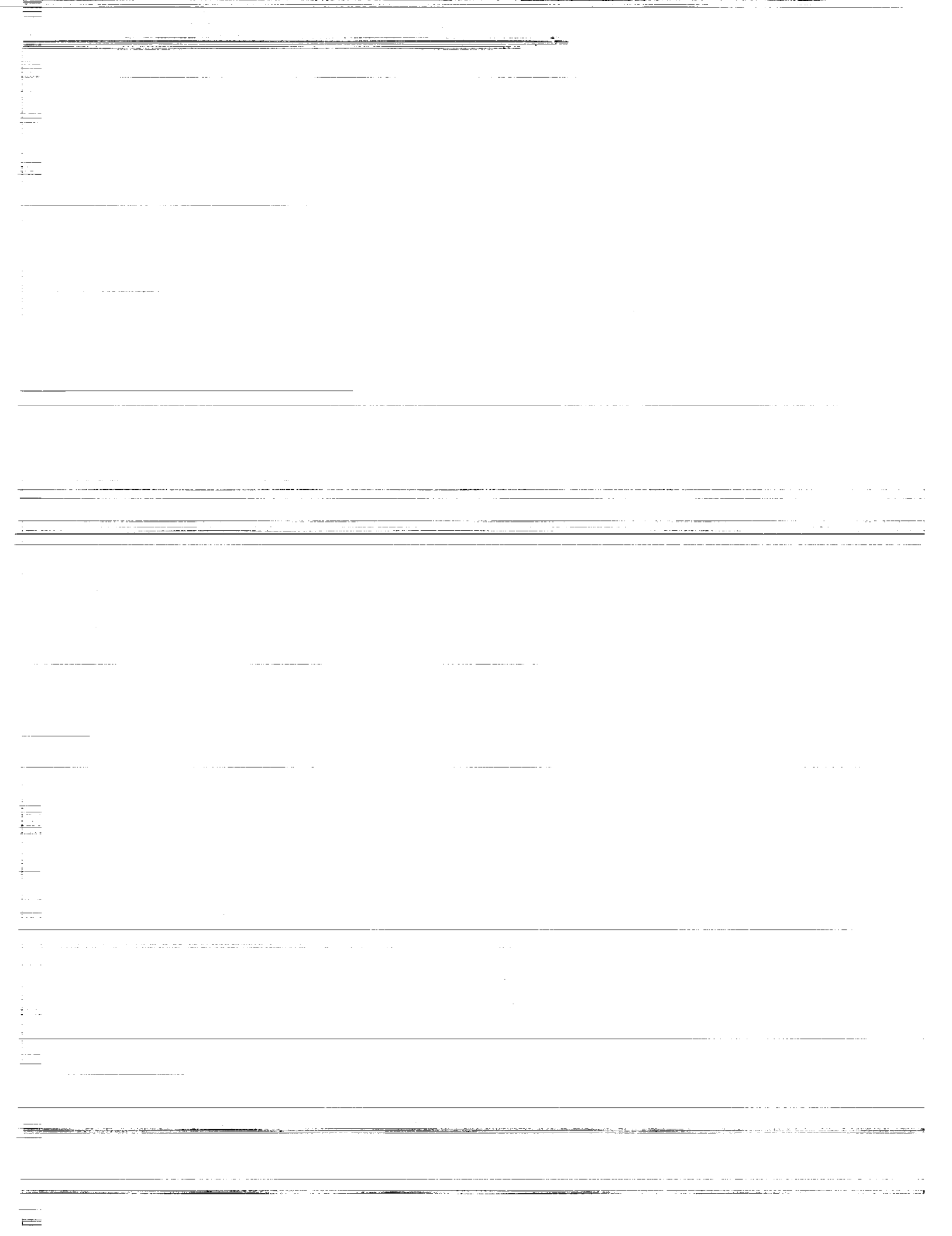

NASA Technical Memorandum 4371

Structural Characterization of a First-Generation Articulated-Truss Joint for Space Crane Application

Thomas R. Sutter, K. Chauncey Wu,
and Kevin T. Riutort
Langley Research Center
Hampton, Virginia

Joseph B. Laufer and James E. Phelps
Lockheed Engineering & Sciences Company
Hampton, Virginia

National Aeronautics and
Space Administration

Office of Management

Scientific and Technical
Information Program

1992

Nomenclature

ASF	assembly and servicing facility
ATJ	articulated-truss joint
ATTB	articulated-truss test-bed
DCDT	direct-current displacement transducers
DOF	degrees of freedom
EA	axial stiffness
EAL	Engineering Analysis Language
EI	bending stiffness
FRF	frequency response function
g	acceleration due to gravity (where $1g \approx 32.174$ ft/sec^2)
PSR	Precision Segmented Reflector
RMS	remote manipulator system
RT	reference truss
VDC	volts direct current

Abstract

A first-generation space crane articulated-truss joint was statically and dynamically characterized in a configuration that approximated an operational environment. The articulated-truss joint was integrated into a test-bed for structural characterization. Static characterization was performed by applying known loads and measuring the corresponding deflections to obtain load-deflection curves. Dynamic characterization was performed using modal testing to experimentally determine the first six mode shapes, frequencies, and modal damping values. Static and dynamic characteristics were also determined for a reference truss that served as a characterization baseline. Load-deflection curves and experimental frequency response functions are presented for the reference truss and the articulated-truss joint mounted in the test-bed. The static and dynamic experimental results are compared with analytical predictions obtained from finite element analyses. Load-deflection response is also presented for one of the linear actuators used in the articulated-truss joint. Finally, an assessment is presented for the predictability of the truss hardware used in the reference truss and articulated-truss joint based upon hardware stiffness properties that were previously obtained during the Precision Segmented Reflector (PSR) Technology Development Program.

Introduction

Manned missions to establish a permanent lunar base and to explore Mars will require new space vehicles and technologies. The large mass and volume required for these space exploration vehicles will probably exceed any available single-launch capability. As a result, it might become necessary to transport vehicle components to an orbiting assembly and servicing facility where final assembly and checkout can be completed (ref. 1). This orbiting facility would be independent of Space Station *Freedom* and would require new technology in automation and robotics, vehicle servicing and processing, fuel transfer and storage, and infrastructure design (ref. 2).

To assemble these large space vehicles, one or more space cranes would provide the capability to precisely manipulate the large and massive vehicle components for final assembly (ref. 3). NASA's current capability for in-orbit payload positioning is the remote manipulator system (RMS), which has been in operation on the Space Shuttle during the last decade. The RMS is a 50-ft-long, six-degree-of-freedom (DOF) manipulator that was specifically designed for deploying and retrieving payloads up to 29 500 kg from the Space Shuttle cargo bay (ref. 4). The RMS has two high-stiffness booms that are connected by relatively flexible rotary joints to form a manipulator. The rotary joints are high-ratio gear boxes that are driven by electrical motors, and the RMS booms are graphite-epoxy tubes. There are six rotary joints in the RMS, and each rotary joint corresponds to one DOF. The articulated-truss space crane concept differs from the RMS and other space crane concepts similar to the RMS (refs. 5, 6, and 7) in that it uses erectable truss technology to provide booms and joints that have high-stiffness properties. The proposed space crane concept also differs from the RMS concepts in that it is reconfigurable, highly controllable, and mounted on a mobile base; also, it will depend heavily upon automation and robotics technologies to assemble the space vehicles.

The objective of this paper is to present static and dynamic test results for the structural characterization of a first-generation articulated-truss space crane joint. For this purpose, a cantilevered articulated-truss test-bed (ATTB) was constructed with one first-generation articulated-truss joint (ATJ). A reference truss (RT), without the ATJ, was also constructed and subjected to identical structural tests. The RT served as a structural characterization baseline for the testing, and it was also used to examine the structural predictability and linearity of the erectable truss hardware. Predictability is an important consideration for large space structures such as the space crane because these structures are often too large to assemble and fully test as a complete system before launch (ref. 2). Analytical results, obtained from finite element models, are compared with experimental results for the static and dynamic tests of the RT and ATTB.

Space Crane Concept

One example of a space crane concept is shown in figure 1. In this figure, the two space cranes are assembling a Lunar Transfer Vehicle and a modular aerobrake at an orbiting assembly and servicing

facility. The space cranes would assemble the Lunar Transfer Vehicle from several large and massive components that have been transported to the assembly and servicing facility by the Space Shuttle. The precise positioning capability of the space crane is used to maneuver and position these large components accurately while astronauts or end effectors make the final connections between the vehicle components. The space crane end effectors are also used to aid in the construction of the modular aerobrake from many small components. End effectors are changed to accomplish specific tasks as required during construction, including final inspection.

In figure 2 another space crane concept is shown that is composed of three truss booms, three identical ATJ's, and a rotary joint (ref. 8). This space crane concept is a four-DOF articulated-truss structure that is 22 m long with a payload range perhaps up to 45 000 kg. Each ATJ provides one-DOF motion in one plane, whereas the rotary joint provides a rotational DOF for out-of-plane motion. Each end effector has six DOF's and is mounted on a mobile base that can be moved along the space crane booms to further increase the work envelope. The three ATJ's and the space crane mobile base provide the coarse positioning capability, whereas the space crane end effectors provide the precise positioning capability needed for component attachment to the space crane for manipulation to a work area. The end effectors, after being positioned at the work area by the crane, perform the assembly operations needed to complete the vehicle. The space crane would be constructed using erectable truss hardware (refs. 9 and 10) to allow configuration changes to the crane, such as adding another truss boom or ATJ. This provides the space crane with additional versatility to meet new construction requirements in orbit. Because the space crane is constructed using an erectable truss structure, it would be transported to the assembly and servicing facility (ASF) in small components. Once at the ASF, the space crane would be erected by astronauts or done robotically.

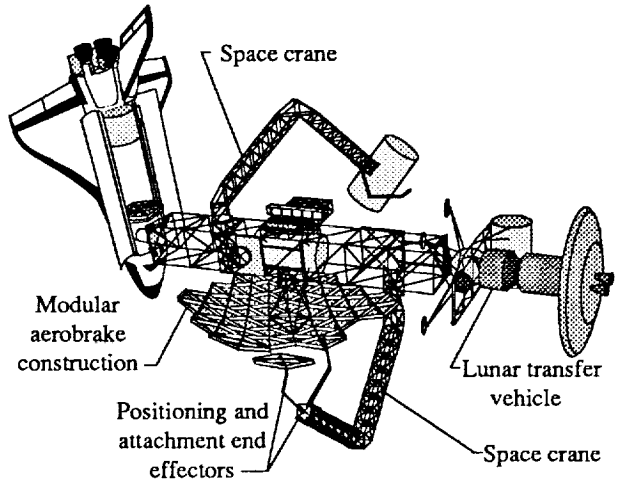

Figure 1. Assembly and servicing facility.

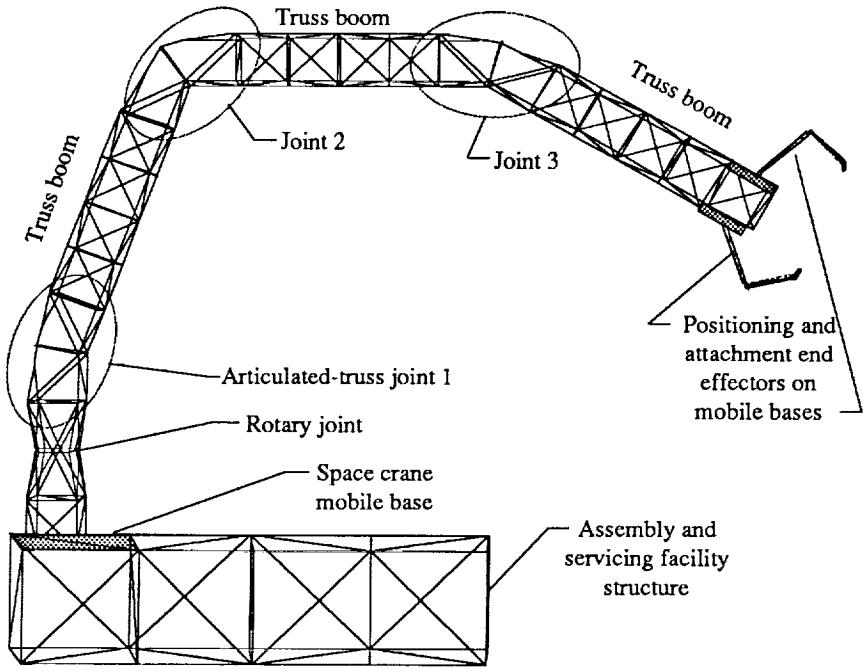

Figure 2. Space crane concept.

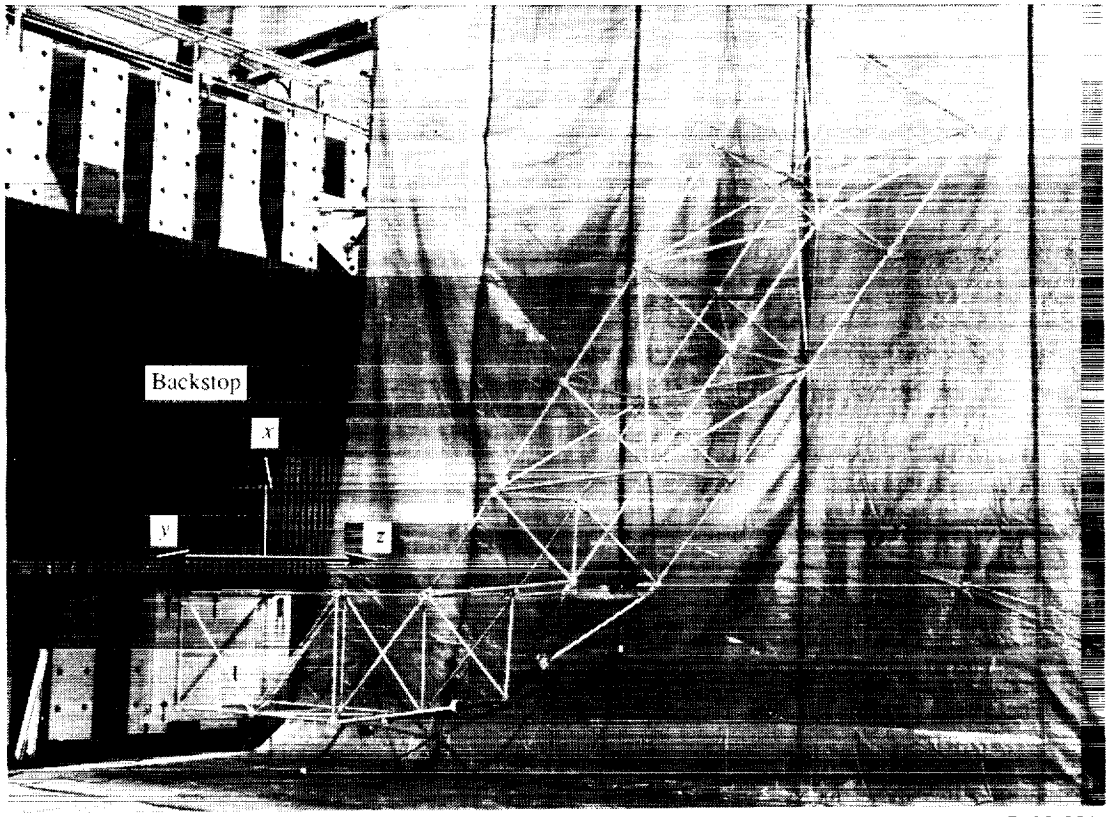

Figure 3. Articulated-truss test-bed.

Articulated-Truss Test-Bed

Figure 3 shows the ATTB structure cantilevered from a rigid, structural backstop. The outer four-bay truss boom has been rotated upward 60° from the horizontal position. The backstop provides a stable and rigid structure to which the test-bed is mounted. The first purpose of the ATTB is to allow different ATJ candidates to be statically, dynamically, and operationally tested. The testing results will lead to a better understanding of the ATJ design issues that will contribute to the selection of the best performing joint for the space crane. The test results will also permit the refinement of finite element models that are used to obtain analytical results. The second purpose is to experimentally evaluate passive damping hardware for potential application with the space crane. Passive damping might be the initial approach to providing the vibration damping needed for the space crane control. Active damping (if needed), in conjunction with passive vibration damping, could be the other approach. The third purpose of the ATTB is to experimentally evaluate open- and closed-loop control laws for large-angle slew maneuvers. Experimental results will be compared with analytical results obtained by simulations. These experiments will be performed with the ATTB operating in the planar configuration that was used to obtain the static and dynamic characteristics presented in this paper.

The ATTB currently consists of a two-bay truss boom and a four-bay truss boom joined by an ATJ. The first-generation ATJ is equivalent to two bay lengths of the truss. A bay is a 1-m cubic section of the truss boom. For the static and dynamic testing presented here, the ATTB is rotated 90° about the z-axis in figure 3. This rotation eliminates the axial loads through the actuators that are due to the weight of the outer truss boom. Because the actuators are not axially loaded, the ATTB static and dynamic testing in this configuration approximates the microgravity environment found in orbit. However, it is recognized that all the effects of gravity cannot be eliminated by testing the ATTB in the rotated configuration. To examine the predictability and repeatability of the erectable truss hardware, an eight-bay RT was used as a structural characterization baseline for the static and dynamic tests. The RT used the same erectable truss hardware as the

ATTB except that the ATJ was replaced with two 1-m truss bays. Thus, the RT is an 8-m truss boom that consists of eight truss bays. The erectable truss hardware, used for the RT and the ATTB, was developed for the Precision Segmented Reflector (PSR) Technology Development Program. This hardware has demonstrated excellent linear structural performance during previous static and dynamic testing (ref. 10).

First-Generation Articulated-Truss Joint

Figure 4 shows the first-generation ATJ in the test-bed structure. The two linear actuators have been extended to effect a 90° bend in the test-bed structure. The ATJ is equivalent to two truss bays in length and is comprised of three double hinges, four single hinges, two actuator support beams (labeled Beam in the figure), two linear actuators, and erectable truss hardware. The single and double hinges allow the ATJ to rotate as the linear actuators are extended. The double hinges are located at the three vertices of the ATJ A-frame. The A-frame serves to maintain the cross-sectional depth of the ATJ as the joint rotates and to stabilize the three double hinges. The A-frame is connected to the two linear actuators at a double hinge. The two actuator support beams are attached to the end of each linear actuator.

The two linear actuators provide the forces needed to rotate the ATJ. The linear actuators are electrically driven, 90-VDC, recirculating ball screws with a static load capacity of 3000 lbf (extendable to 36 in.) and are rated to apply loads up to 1500 lbf. The actuator extension velocity is variable from 0.02 to 0.20 in/sec, thus allowing the ATTB to be rotated to 120° in approximately 2.5 minutes at the maximum extension velocity. The actuator mass is approximately 26 lbm. These actuators are relatively low-fidelity inexpensive devices chosen primarily to evaluate the kinematic and operational performance of the ATJ, and they are not flight quality or the best available. The ATTB static and dynamic testing was initiated with these actuators because they were on hand. Future plans are to replace these actuators with higher fidelity devices.

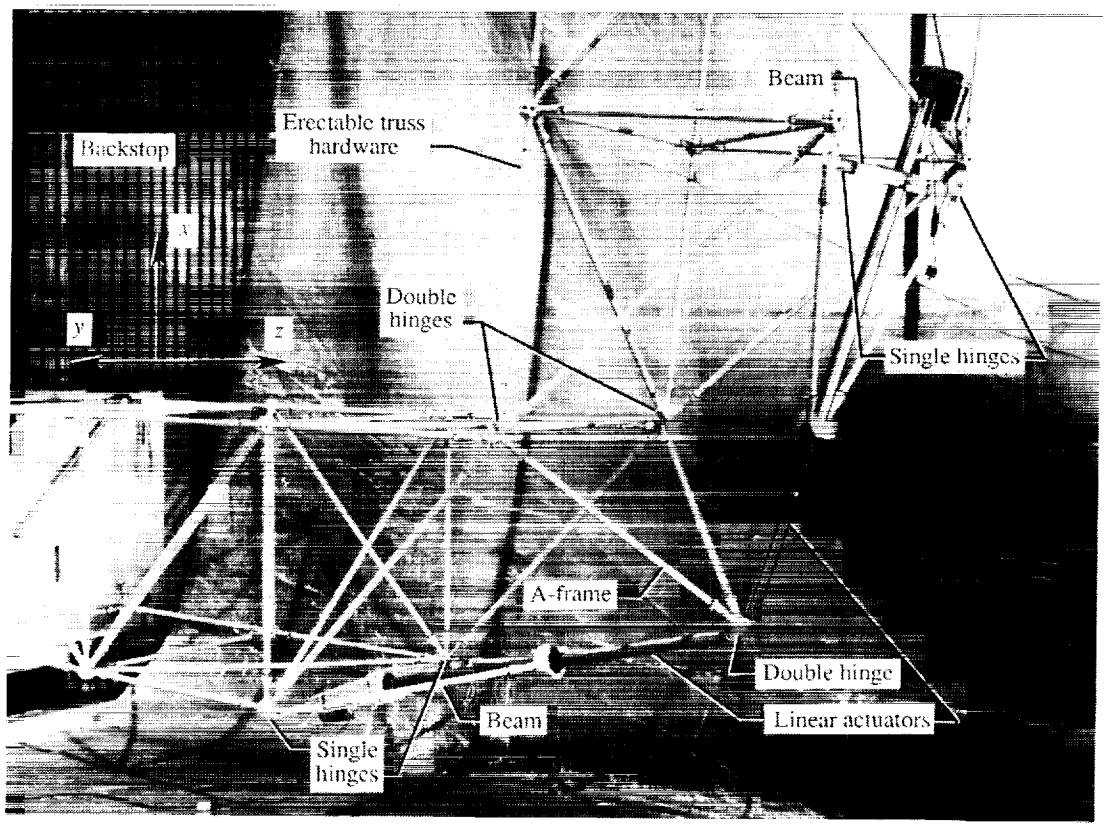

L-92-330

Figure 4. First-generation articulated-truss joint.

Actuator Load-Deflection Tests

The actuator axial stiffness characteristics were determined by experimentally obtaining load-deflection curves at several extension lengths. One of the two actuators was selected for testing at extension lengths of 6, 12, 18, 24, and 29 in. The purpose of the test was to obtain experimental axial stiffness values for use in a linear finite element analysis of the ATTB. The actuator test setup is shown in figure 5(a). A load cell, shown attached between the lower end of the test fixture and the lower crosshead of the test machine, was used to measure the applied force. Three direct-current displacement transducers (DCDT's), shown located at 120° intervals around the longitudinal axis of the actuators at the upper end, were used to measure the corresponding displacements. These displacements were due to the axial deformation of the actuator. The DCDT's were placed between the top of the test fixture and the top crosshead of the test machine as shown in figure 5(b).

The actuator was rigidly attached to the top of the test fixture, and the actuator pin hinge was connected to the top crosshead of the test machine. (See fig. 5(b).) The actuator was loaded to 1500 lbf in tension, unloaded through 0 to 1500 lbf in compression, and then unloaded to 0 lbf to complete one load-deflection curve. The load cycle was then repeated at each actuator extension length to obtain a second load-deflection curve. The load range was chosen because it was representative of the actuator loads expected during subsequent ATTB testing. The axial load and displacement data from the load cell and DCDT's were collected on a data acquisition system and reduced to obtain load-deflection curves for each actuator extension length.

The test fixture was designed to test the axial stiffness properties of the actuators. In figure 6(a) an actuator cross section is shown, and in figures 6(b) and 6(c) an actuator is shown mounted in the ATJ and in the test fixture, respectively. For the load-deflection tests, the load path through the actuator is as follows (see fig. 6(a)): axial loads are applied to point A, and then they follow the inner tube through the ball nut and are transferred to the outer tube near the mounting trunnion. The loads then follow the outer tube back toward point A, and they are reacted to the test fixture or the ATJ at point B. From point B, the struts react the loads to the truss nodes in the ATJ as shown in figure 6(b). When the actuator is mounted in the test fixture, the loads are reacted from point B on the test fixture to the test machine at point C as shown in figure 6(c). The actuator motor and gear housing are not in the structural load path, and the actuators were not tested with shear loads or bending moments applied in addition to the axial loads. The test fixture was fabricated from ASTM A36 structural carbon-steel plate and had an axial stiffness of approximately 2.0×10^6 lbf/in., which is much larger than the stiffness of the actuator.

A typical experimental actuator load-deflection curve is shown in figure 7 for one actuator at an extension length of 6 in. The load-deflection curve exhibited significant backlash as evidenced by the large deflections resulting from small load increments in the vicinity of a −150-lbf applied load. However, the load-deflection response was approximately linear for compressive loads greater than 150 lbf and for tensile loads. The occurrence of backlash in the region of −150 lbf was believed to be attributable to a preload in the actuator. The actuator axial stiffness (at an extension length of 6 in.) was approximately 91 000 lbf/in. and was obtained from the slope of these segments of the load-deflection response. The actuator backlash was exhibited in the subsequent load-deflection testing of the ATTB, which is described in a later section. Load-deflection tests were completed for the remaining actuator extension lengths; and the actuator axial stiffness values were determined at each length tested to obtain the actuator stiffness as a function of extension length.

The backlash amount was not constant over the extension range and was approximately 0.06, 0.06, 0.14, 0.14, and 0.14 in. for actuator extension lengths of 6, 12, 18, 24, and 29 in., respectively. The backlash values were not consistent as the length was increased to 18 in. and beyond, which suggests that the backlash was not repeatable. The primary source for the backlash was believed to be attributable to the clearance between the ball bearings, ball nut, and ball screw, as shown in figure 8. One approach to reducing the backlash was to replace the ball bearings with larger diameter ball bearings. This approach was subsequently used to reduce the actuator backlash. New actuators were obtained with the larger diameter ball bearings installed, and they are referred to as *improved actuators* in the remainder of this paper. The "unimproved" actuators are subsequently referred to as the *original actuators*. The improved actuators have the same load, extension velocity, and stiffness specifications as the original actuators. Other approaches to reduce backlash, such as using two preloaded ball nuts, are under consideration but have not been implemented.

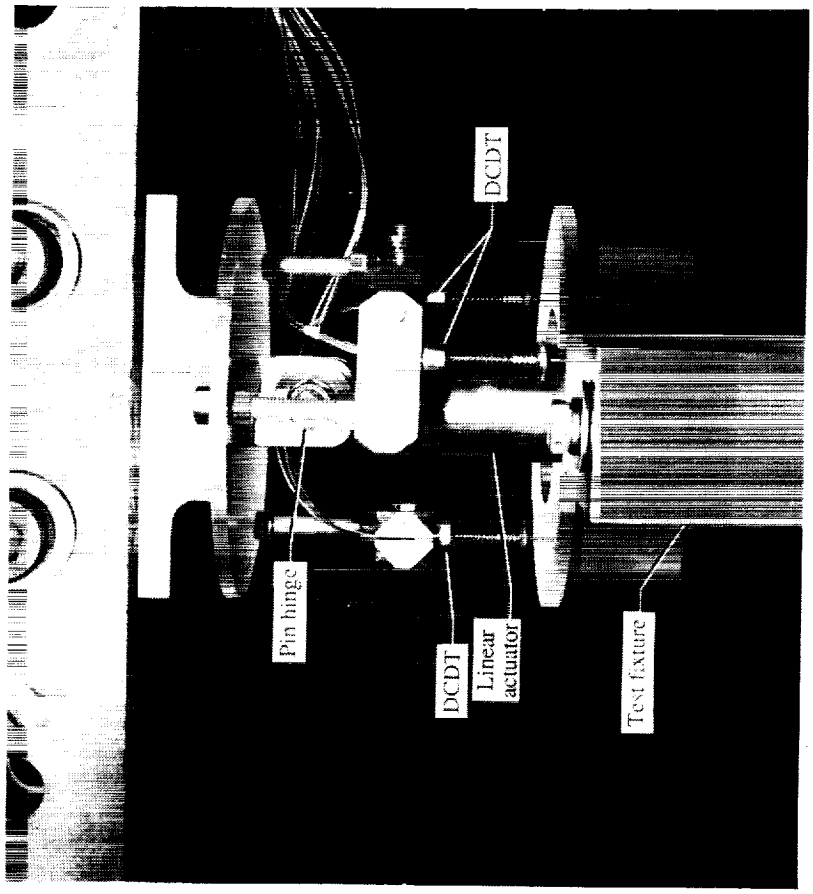

(b) DCDT's located at top of test fixture (side view).

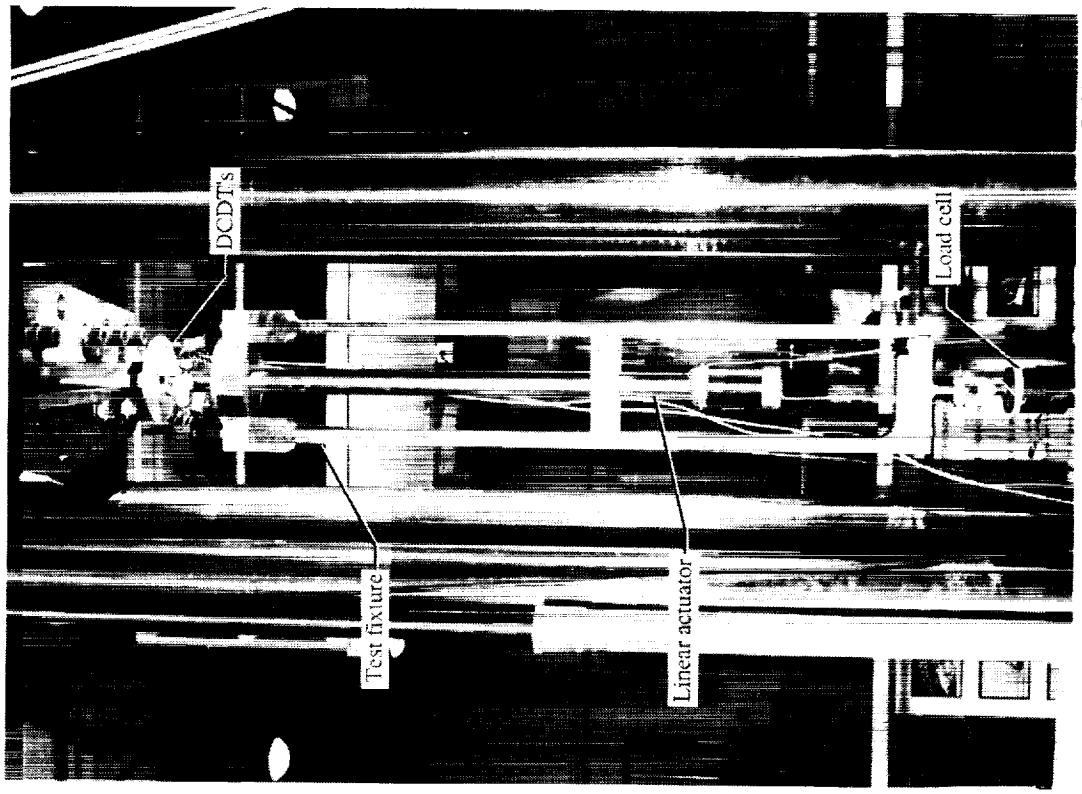

(a) Actuator mounted in test fixture.

Figure 5. Test setup used to determine actuator stiffness.

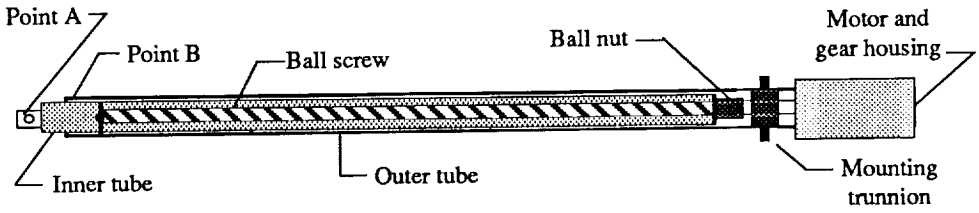

(a) Actuator cross section.

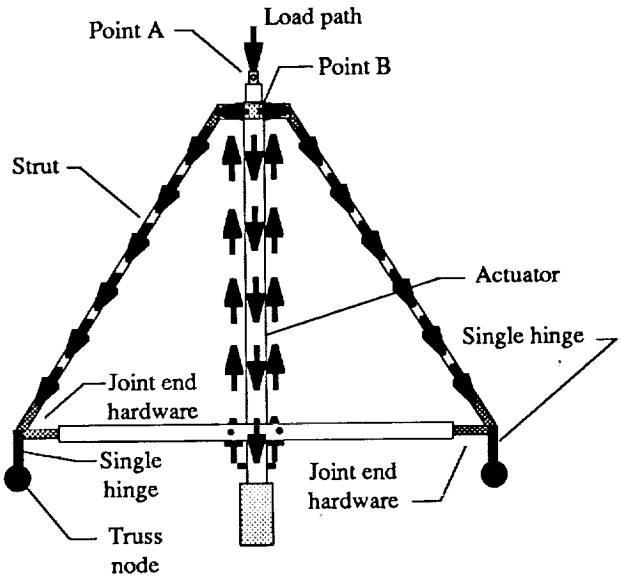

(b) Actuator mounted in articulated-truss joint.

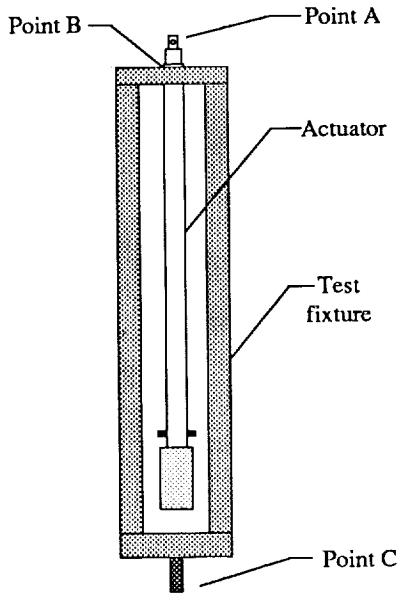

(c) Actuator mounted in test fixture.

Figure 6. Comparison of actuator load paths.

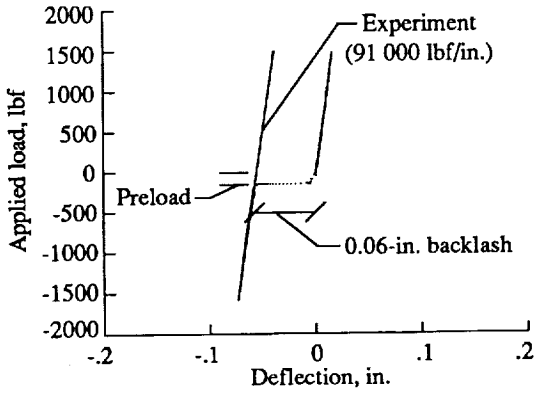

Figure 7. Actuator load-deflection curve at extension length of 6 in.

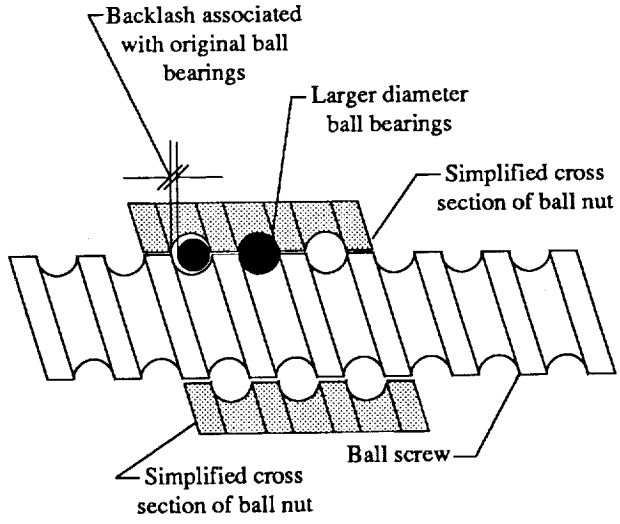

Figure 8. Schematic of ball screw and ball nut.

The actuator axial stiffness values are plotted in figure 9 as a function of the actuator extension lengths tested. A linear best-fit curve is also shown, and, as expected, the actuator stiffness decreased almost linearly as the extension length increased. The purpose of determining the actuator stiffness as a function of extension length was to provide sufficient data to estimate the actuator axial stiffness over the extension range. This allows testing of the ATTB at several different rotation angles. The actuator stiffness was incorporated in a linear finite element model by defining the axial stiffness of the finite element representing the actuator to be equal to the experimentally determined axial stiffness value at the appropriate extension length.

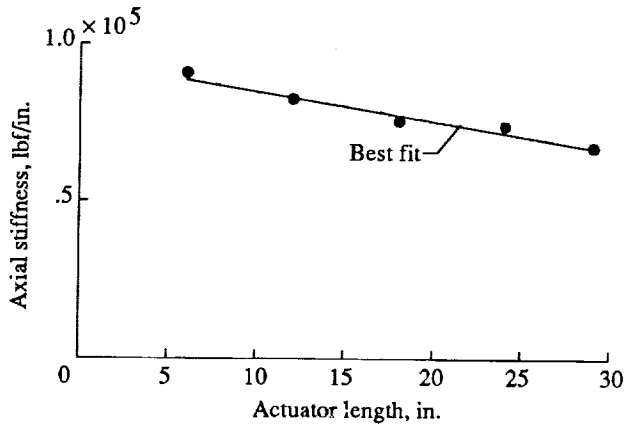

Figure 9. Actuator stiffness as a function of actuator extension length.

Finite Element Representation

The Engineering Analysis Language (EAL) was the finite element program used to model the RT and ATTB. (See ref. 11.) In figure 10 the RT finite element model is shown with a detail of a typical strut model. The struts are further denoted as *longerons, diagonals,* and *battens.* Each strut was modeled using six beam elements: four equal-length beam elements represented the strut tube, and one beam element represented each joint end hardware. The strut tube section and mass properties were derived from a 0.058-in. wall-thickness aluminum tube with an outside diameter of 1 in. and with a material density of 0.1 lbm/in^3. The joint end hardware had an experimentally determined (ref. 10) axial stiffness (EA) of 1.9×10^6 lbf, a major axis bending stiffness (EI) of 1.55×10^5 lbf-in^2, and a minor axis bending stiffness of 1.26×10^5 lbf-in^2. These sectional stiffness properties were used to calculate the corresponding section properties of the beam element representing the joint end hardware. The joint length was 5.56 in. as indicated in figure 10. The joint hardware at each strut end had a mass of 0.44 lbm, which was modeled as a lineal mass along the length of the element representing the joint end hardware. Each truss node mass was modeled as a 0.8-lbm point mass. The number of struts (and hence the joint end hardware) connected to each truss node is denoted as the node connectivity in figure 10. The greater the node connectivity, the higher the corresponding total mass is at a truss node.

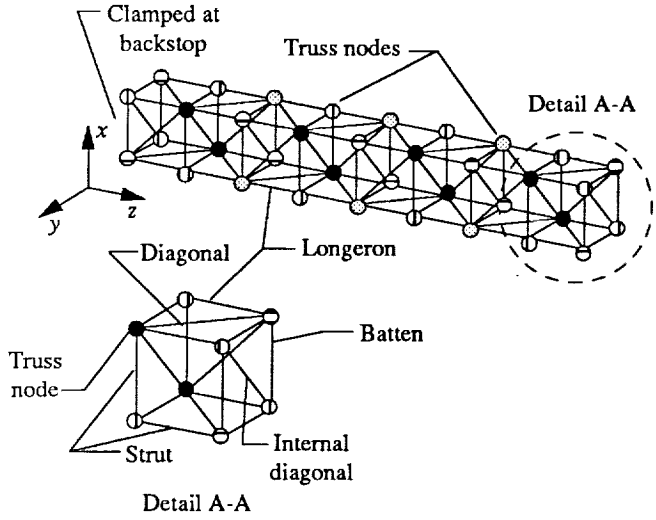

(a) Strut connectivity for RT.

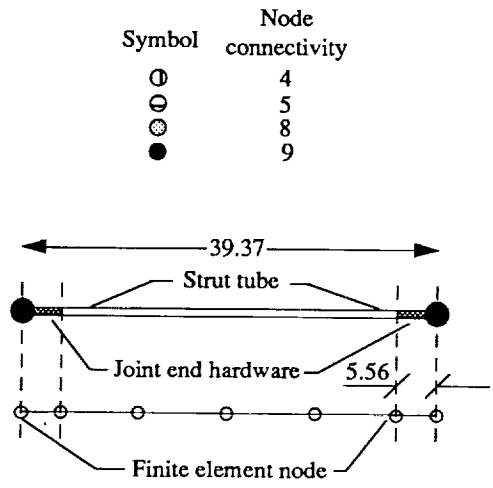

(b) Representation of typical strut finite element.

Figure 10. Detail of RT finite element model. Linear dimensions are given in inches.

The ATTB struts were modeled in the same manner as those for the RT. In figure 11 the finite element detail of the ATJ is shown in the same orientation as that shown in figure 4. The ATJ struts are shown as dashed lines. The linear actuators were modeled using beam elements with the experimentally determined axial stiffness value corresponding to the appropriate extension length. The actuator inner tube bending, shear, and torsion stiffness values were estimated from the section properties of a 0.125-in. wall-thickness tube with an outside diameter of 1.75 in., and the corresponding outer tube properties were estimated from the section properties of a 0.125-in. wall-thickness tube with an outside diameter of 2 in. The actuator mass was modeled as a lineal mass distributed along the length of the actuator.

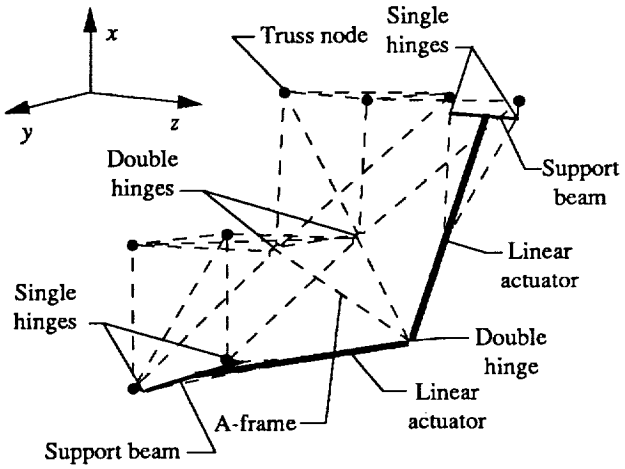

Figure 11. Detail of finite element model of ATJ.

The rotational DOF's, corresponding to each hinge, were released at the finite element node representing the hinge. The hinge mass was modeled as a point mass. The actuator support beams were modeled using the section properties of a wide flange beam having a flange width of 1.25 in., a thickness of 0.25 in., and a web height and thickness of 3.5 in. and 0.125 in., respectively. The actuator support beam mass was modeled as a lineal mass distributed along the length of the beam element. The RT and ATTB finite element analyses included the effect of geometric stiffness (ref. 12) because of the gravity loading.

Static Characterization

The RT and ATTB were cantilevered from a rigid backstop as shown in figure 12 for the ATTB. A linear actuator was used to apply the forces to the RT and ATTB, a load cell was used to measure the applied forces, a load bar was used to transfer the loads from the actuator to two truss nodes, and DCDT's were used to measure the corresponding displacements. The plane of the floor was in the yz-plane, and the gravity vector was in the $-x$-direction. The applied forces and displacements were used to obtain a load-deflection curve for the RT and also for the ATTB with the original actuators, improved actuators, and, finally, steel tubes (zero backlash) in place of the actuators. The ATTB was tested at a joint rotation angle of 0° to obtain a configuration comparable to the RT. Analytical predictions, obtained from the corresponding finite element models, are presented for the RT and ATTB.

Reference Truss

A schematic of the RT static test configuration is shown in figure 13 along with the applied force and the displacement measurement locations. The RT was loaded to 270 lbf, unloaded through 0 to −269 lbf, and then unloaded to 0 lbf to complete one cycle. This cycle was repeated three times to obtain the load-deflection curve shown in figure 14. The load-deflection curve was linear with little or no discernible hysteresis, which indicated a well-behaved and linear structure over the entire load range. The load-deflection curve slope was approximately 445 lbf/in., which compared well with an analytical slope of 446 lbf/in. obtained from the RT finite element model. This good correlation between the experimental and analytical slopes suggests excellent predictability and linearity for the PSR-type hardware used in the RT.

In figure 15 the analytical deformed shape is shown for a −269.32-lbf load applied at the location indicated in figure 13. The corresponding y-displacement was −0.604 in. The deformed shape was multiplied by a scale factor so that the deformations would be apparent in the figure. This loading condition introduced unsymmetrical bending because the bending axis did not coincide with either principal axis of inertia (x' or y') for this strut lacing pattern. (See fig. 10.) The total x-displacement was approximately −0.270 in. at the y-deflection measurement location, with −0.252 in. attributable to gravity. The x-displacement due to unsymmetrical bending was approximately −0.0178 in., which is approximately 3 percent of the y-displacement (−0.604 in.). The total strain energy was calculated for this deformed shape, and the percent of strain energy was determined for axial, bending, torsion, and shear deformations in the beam elements representing the truss struts (ref. 13). Of the total strain

energy, 99 percent was due to the axial deformation, which indicated that the RT was behaving as a truss because the primary forces in the structure were the axial forces. Practically no torsion, shear, or bending forces were apparent in the struts as indicated by the strain energy calculations.

Articulated-Truss Test-Bed

A schematic of the ATTB in the straight configuration is shown in figure 16. The force was applied and displacements were measured at the same locations as those used for the RT. The original actuators were used for this test, and they were extended approximately 5 in. in this configuration. The load-deflection curve is shown in figure 17. The ATTB was loaded to 220 lbf, unloaded through 0 to −251 lbf, and then unloaded to 0 lbf to complete the load-deflection curve. This load-deflection curve indicated a nonlinear behavior for applied forces in the 0- to 50-lbf range; but as the applied force was increased beyond this range, the load-deflection curve became approximately linear. The nonlinear behavior was expected because of the nonlinear actuator load-deflection curves. (See fig. 7.) The total backlash was estimated to be 0.21 in. as shown in the load-deflection curve; this includes the backlash in the actuators as well as the single and double hinges of the ATJ which have not been tested.

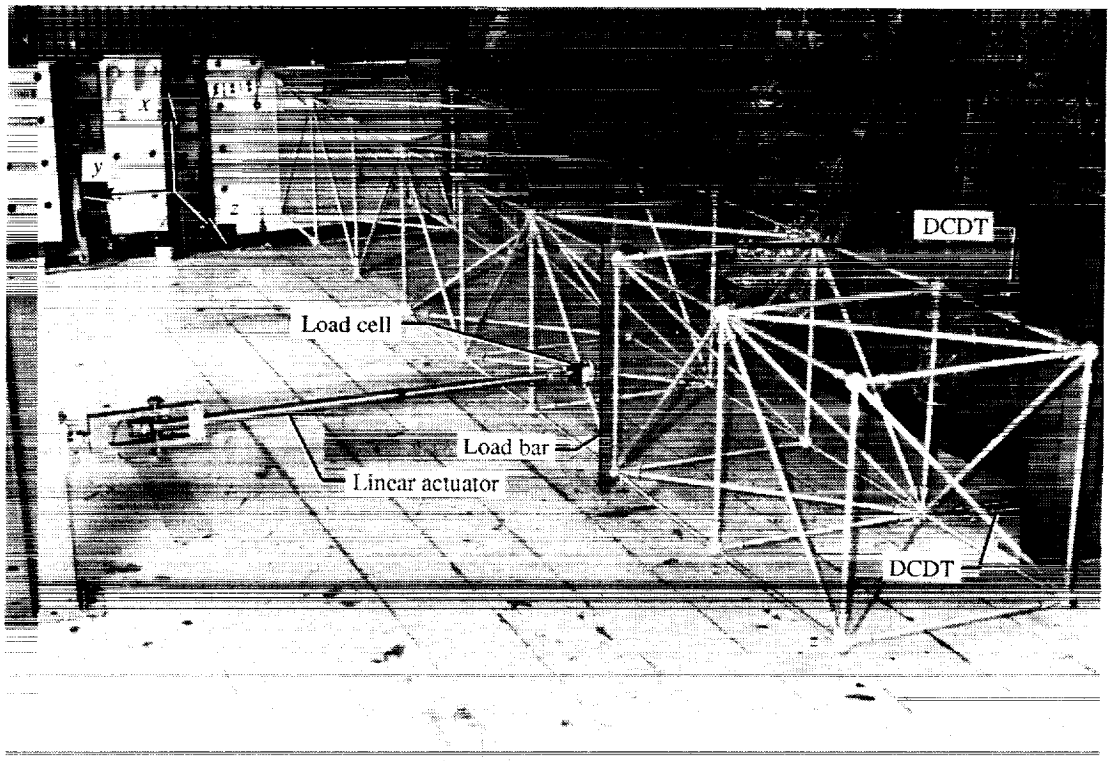

L-91-04278

Figure 12. Test setup used for static testing of RT and ATTB. (ATTB is shown.)

The behavior in the region of low applied loads did not appear to exhibit the suspect preload in the actuator, and the exact reason was not clear. However, the analysis indicated relatively large shear loads in the actuators, which might have changed their behavior in this region. The slope of the load-deflection curve was approximately 261 lbf/in. and was obtained from the slope of the load-deflection curve outside the backlash region as shown in the figure. This represents a 41-percent reduction in slope compared with the RT. An analytical slope of approximately 309 lbf/in. was obtained from the ATTB finite element model, which was 18 percent greater than the experimentally determined value. The actuator backlash was not included in the linear finite element analysis. The difference in analytical and

experimental results suggests that experimental stiffness testing is required for the remaining components of the ATJ such as the double and single hinges.

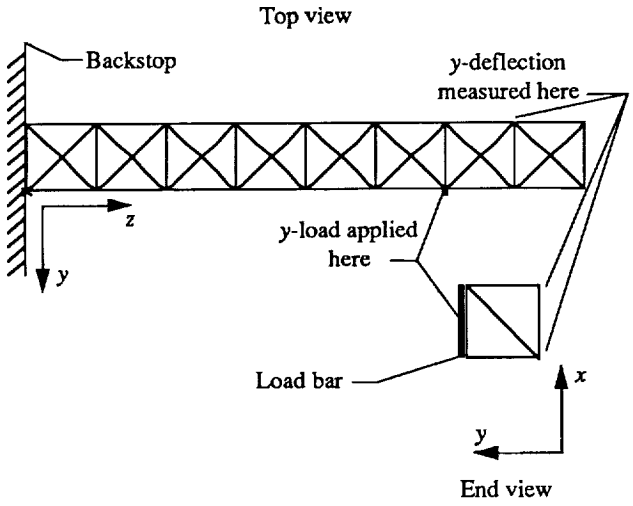

Figure 13. RT static test configuration.

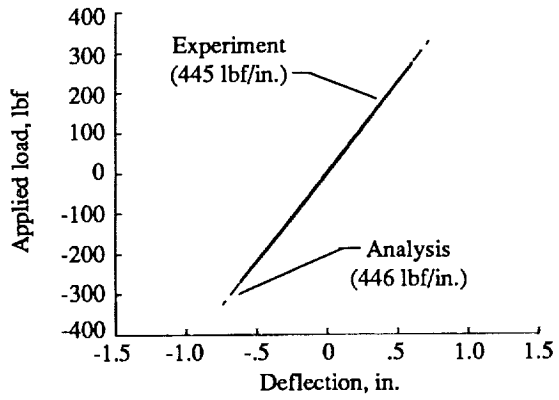

Figure 14. Load-deflection curve for RT.

In figure 18 the analytical deformed shape is shown for a -251.50-lbf load applied at the location indicated in figure 16. The corresponding y-displacement was -0.815 in. The deformed shape was multiplied by a scale factor so that the deformations would be apparent in the figure. Also shown in the figure is an enlarged view of the deformed shape in the vicinity of the ATJ. The ATTB is bending about the x-axis because of the applied load, as shown in the top view. The deformation in the $-x$-direction is primarily due to gravity. The total strain energy was also calculated for this deformed shape, and then the percent of strain energy was determined for bending deformations in the beam elements representing the ATTB. Of the total strain energy, 10 percent was due to the bending deformation in the ATJ elements. The A-frame, ATJ diagonals, and actuator support beams had 8 percent of the total strain energy due to bending, and the ATJ longerons and hinges had the remaining 2 percent. The bending strain energy effect can be seen in the deformed shape of the ATJ which is shown in the enlarged view of figure 18. Bending occurred primarily as a result of load path eccentricities introduced by the double hinges in the A-frame. The ATTB strain energy distribution was different from that of the RT because of the large bending strain energy in the ATJ. The strain energy data suggest that bending characterization of the ATJ components, in addition to axial characterization, is warranted.

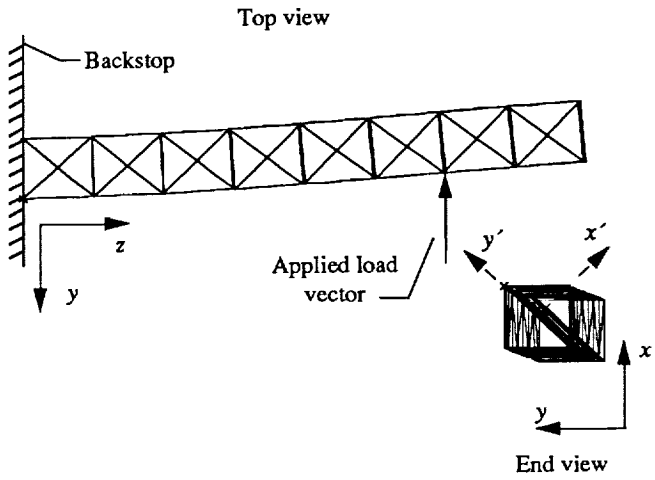

Figure 15. Static deformation obtained from RT finite element model.

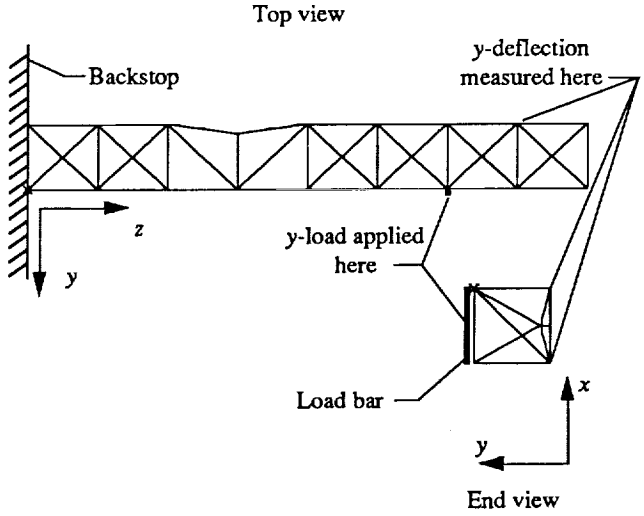

Figure 16. ATTB static test configuration.

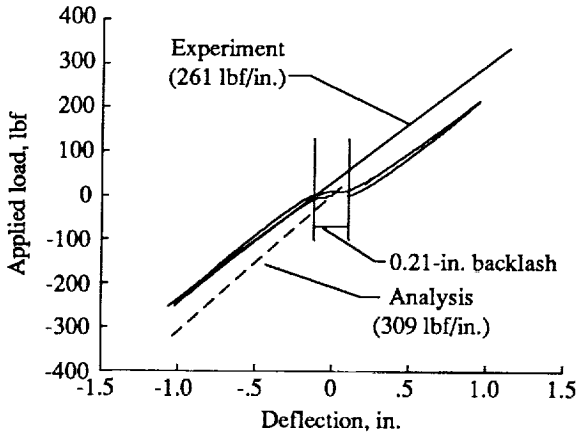

Figure 17. Load-deflection curve for ATTB with original actuators.

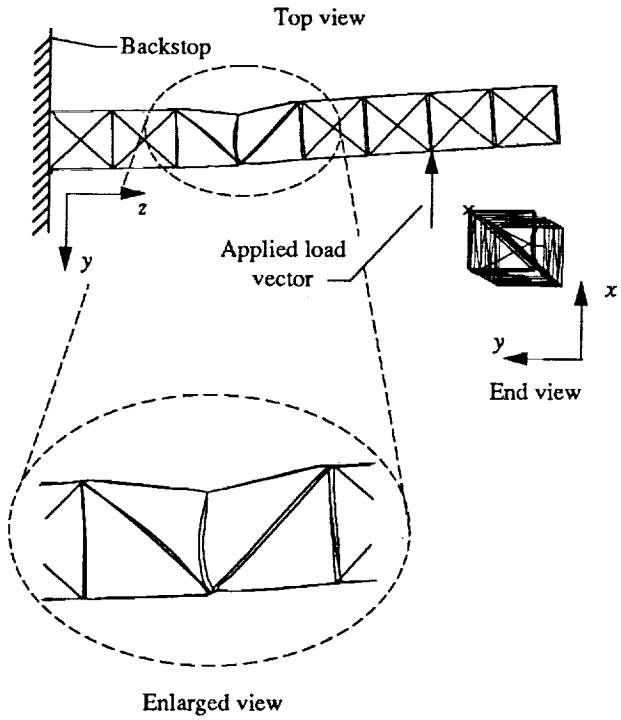

Figure 18. Static deformation obtained from ATTB finite element model.

The ATTB load-deflection test was repeated using the improved actuators in place of the original actuators. The improved actuators are new actuators that have the same load, extension velocity, and stiffness specifications as the original actuators, but the amount of actuator backlash was reduced by using larger diameter ball bearings in the recirculating ball screw, as previously indicated in figure 8. The ATTB was loaded to 280 lbf, unloaded through 0 to −280 lbf, and then unloaded to 0 lbf to complete one cycle. This cycle was repeated three times to obtain the load-deflection curve shown in figure 19. The nonlinearity (backlash) of the load-deflection curve was reduced by 57 percent compared with the previous test results of figure 17 (0.21 in. versus 0.09 in.). Using the improved actuators, the slope of the load-deflection curve was approximately 258 lbf/in., which was within ±1 percent of the slope determined for the ATTB with the original actuators. This agreement in load-deflection slopes was expected because the improved actuators have the same stiffness properties as the original actuators.

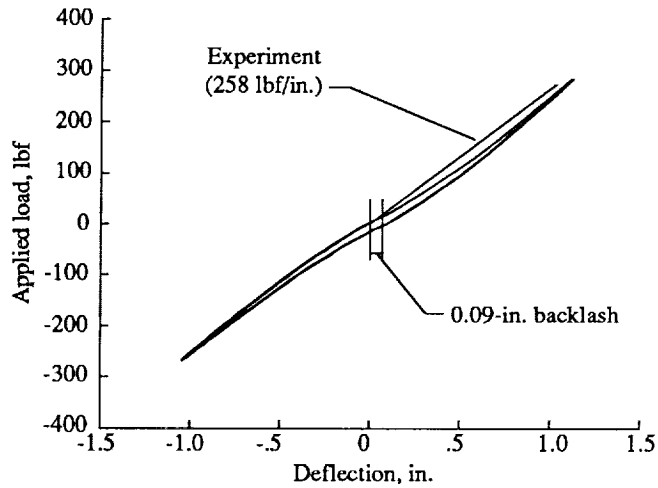

Figure 19. Load-deflection curve for ATTB with improved actuators.

A third load-deflection test was performed on the ATTB to determine the amount of backlash in the ATJ hinges by replacing each actuator with a 0.25-in. wall-thickness steel tube with a 2-in. outside diameter. The axial stiffness of the steel tube was not matched to the original actuators because the purpose of the test was to determine the backlash associated with the hinges. The ATTB was loaded to 280 lbf, unloaded through 0 to −305 lbf, and then unloaded to 0 lbf to complete one cycle. This cycle was repeated three times to obtain the load-deflection curve shown in figure 20, which exhibits a substantial improvement in linearity over the entire load range. The structural backlash was approximately 0.05 in., which was a 44-percent reduction in total backlash compared with that of the ATTB with the improved actuators. The 0.05-in-backlash amount was still substantially larger than that observed with the RT. (See fig. 14.) This suggests that load-deflection testing of the single and double hinges is needed.

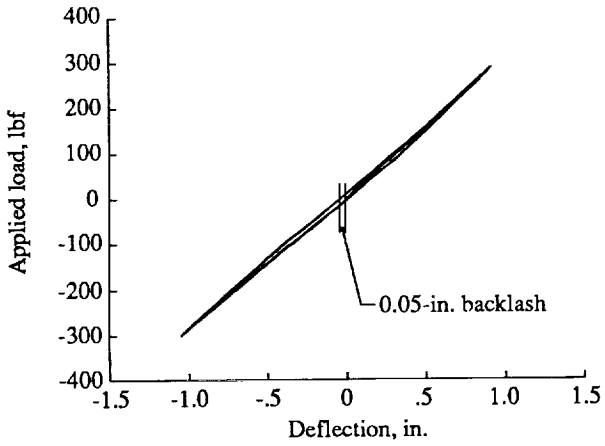

Figure 20. Load-deflection curve for ATTB with steel tubes.

Dynamic Characterization

The RT and ATTB were cantilevered from a rigid backstop, and their dynamic characteristics were experimentally determined using a 16-channel GenRad 2515 data acquisition system (ref. 14) and the Modal-Plus Program of the Structural Dynamics Research Corporation (ref. 15). The modal testing used 14-channels: 1 channel for each of the 2 vibration exciters, and the remaining 12 channels for 4 triaxial accelerometers. The four triaxial accelerometers were relocated along the RT and ATTB truss nodes to obtain experimental frequency response functions (FRF's) in the x-, y-, and z-directions. The two vibration exciters applied random excitation with a root-mean-square force of approximately 1.0 lbf each. The ATTB was tested at a joint rotation angle of 0° to obtain a configuration comparable to the RT. The first six analytical and experimental mode shapes, frequencies, and modal damping values are presented for the ATTB. The ATTB frequencies and modal damping values are compared with the respective RT frequencies and damping values for the corresponding modes. The RT and ATTB analytical dynamic characteristics were obtained from the finite element models used to obtain static predictions.

Reference Truss

In figure 21 the first three analytical mode shapes are plotted for the RT. The fundamental mode shape is shown in figure 21(a) and occurred at a frequency of 6.77 Hz. This mode shape was primarily characterized as a first bending mode about the x'-axis. (See the end view.) The second mode shape is shown in figure 21(b) and occurred at a frequency of 7.02 Hz. This mode shape was characterized as a first bending mode about the y'-axis. These mode shapes indicate bending about the x'- and y'-axes because these are the principal axes of inertia for this strut lacing pattern. (See fig. 10.) The third mode shape is shown in figure 21(c) and occurred at a frequency of 24.41 Hz. This mode was characterized as a first torsion mode about the z-axis.

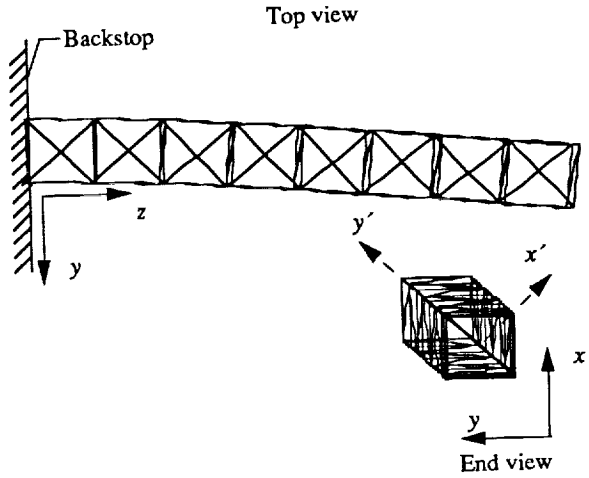

(a) Mode 1 at 6.77 Hz.

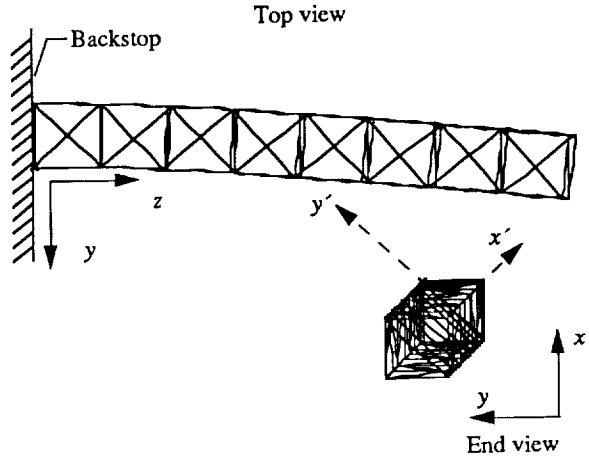

(b) Mode 2 at 7.02 Hz.

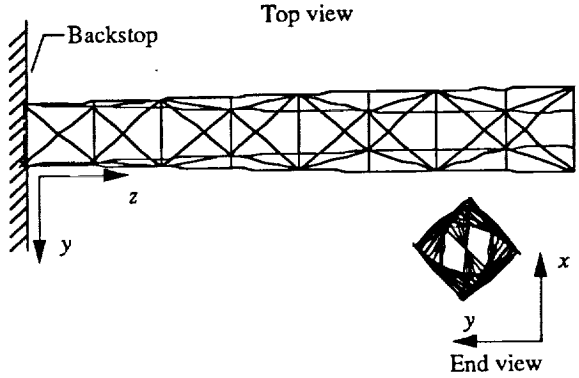

(c) Mode 3 at 24.41 Hz.

Figure 21. First three RT analytical mode shapes.

The RT is shown in figure 22 with the locations indicated for the vibration exciters and truss nodes used in the modal analysis. Vibration exciter 1 applied random forces in the x-direction, and vibration exciter 2 applied the random forces in the y-direction. (See the end view in fig. 22.) Also indicated in the figure is the location of node A where the acceleration time response was measured for one specific FRF that will be discussed subsequently. Experimental RT frequencies were obtained from the frequency response functions, and the experimental mode shapes were obtained using the commercial modal analysis software.

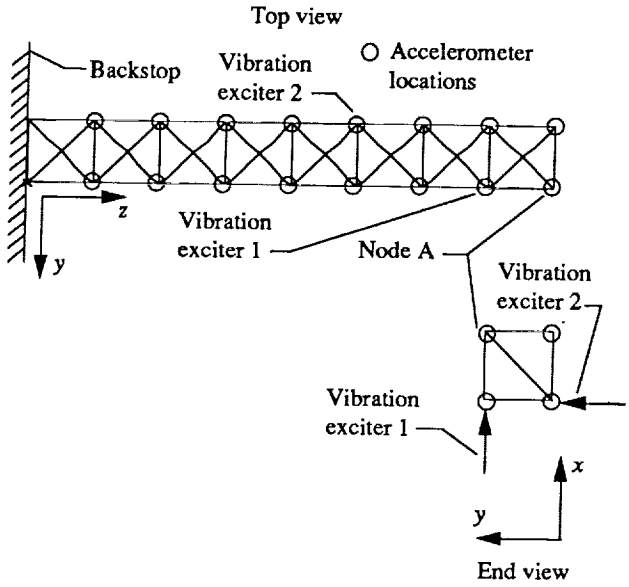

Figure 22. RT dynamic test configuration.

The magnitude component of a typical experimental FRF is shown in figure 23 with three distinct peaks. This FRF corresponds to the y-acceleration time response of node A (see fig. 22) due to random forces applied in the y-direction by vibration exciter 2. The three peaks indicate three distinct modes at 6.79, 7.00, and 24.84 Hz, which correspond to a first bending mode about the x'-axis (see fig. 21), a first bending mode about the y'-axis, and a first torsion mode about the z-axis, respectively. The experimental mode shapes were plotted and then individually compared with the analytical mode shapes to verify matching modes at the respective frequencies.

In table 1, the first six analytical and experimental frequencies are listed along with the percent of difference in frequency between experiment and analysis, a mode shape description, and corresponding modal damping values. The first two experimental frequencies agreed within ± 0.3 percent of the corresponding analytical predictions, the third frequency agreed within ± 1.7 percent, and the remaining frequencies were within ± 1.6 percent of the corresponding analytical predictions. The RT hardware had a very low level of damping as evidenced by the low modal damping values (less than 0.8 percent). The good correlation between experimental and analytical data confirms that the RT dynamic behavior is predictable.

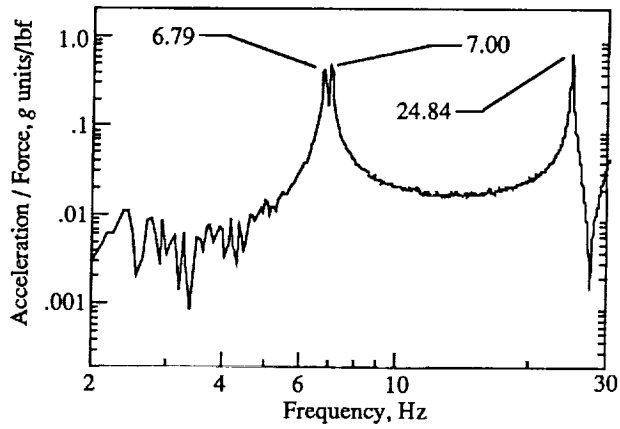

Figure 23. Sample experimental frequency response function for RT.

Table 1. Comparison of Analytical and Experimental Frequencies for the Reference Truss (RT)

Mode	Frequency, Hz		Difference, percent	Mode shape description	Modal damping, percent
	Analytical	Experimental			
1	6.77	6.79	0.3	First bending	0.54
2	7.02	7.00	−.3	First bending	.56
3	24.41	24.84	1.7	First torsion	.40
4	31.38	31.88	1.6	Second bending	.75
5	32.93	33.15	.7	Second bending	.61
6	46.60	47.18	1.2	First axial	.78

Articulated-Truss Test-Bed

Analytical mode shapes were obtained using the finite element model of the ATTB, and they are shown in figure 24. The backlash in the actuators was ignored in the linear finite element analysis. The fundamental mode (shown in fig. 24(a)) occurred at a frequency of 5.52 Hz, which was approximately an 18-percent reduction compared with the first analytical frequency of the RT. This mode shape was primarily characterized as a first bending mode about the x-axis. The second mode shape is shown in figure 24(b) and occurred at a frequency of 5.76 Hz. This frequency represented an 18-percent reduction compared with the second analytical frequency of the RT. The corresponding mode shape was primarily characterized as a first bending mode about the y-axis. These first bending mode shapes are different from the corresponding RT first bending mode shapes because of the difference in the stiffness and mass properties of the ATJ located between the two booms. The third analytical mode shape was a first torsion mode about the z-axis, as shown in figure 24(c). This mode occurred at a frequency of 15.34 Hz, which was a 37-percent reduction compared with the first torsion frequency of the RT. The first three frequencies of the ATTB were lower than the corresponding frequencies of the RT because of the reduction in bending and torsion stiffness properties of the ATJ.

The ATTB is shown in figure 25 with the locations indicated for the vibration exciters and truss nodes used in the modal testing. For this testing, additional accelerometers were also located on the ATJ to obtain data on the acceleration time response. The dynamic characteristics of the ATTB with the original actuators installed were determined for the straight configuration as shown in the figure. Also indicated in figure 25 is the location of node A where the acceleration time response was measured for two specific FRF's that will be discussed subsequently. Vibration exciter 1 applied the random forces in the x-direction, and vibration exciter 2 applied random forces in the y-direction. (See end view in fig. 25.) The vibration exciter force levels (approximately 1.0 lbf root mean square) used during the ATTB modal testing were substantially lower than required to force the actuators into their nonlinear (i.e., backlash-dominated) regions. As a result, the ATTB behaved as a structure without the highly nonlinear performance discovered during the actuator load-deflection testing. The ATTB would not be expected to exhibit this linear behavior if larger excitation forces were used.

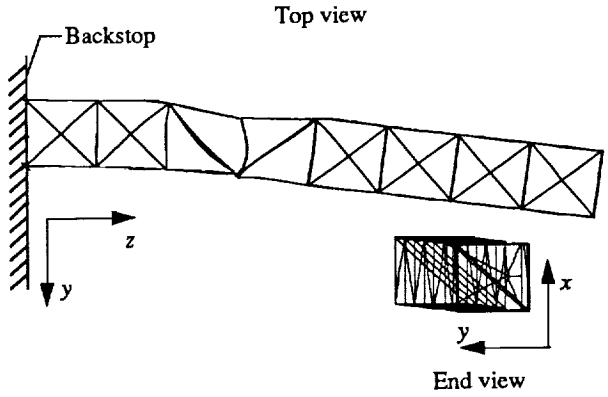

(a) Mode 1 at 5.52 Hz.

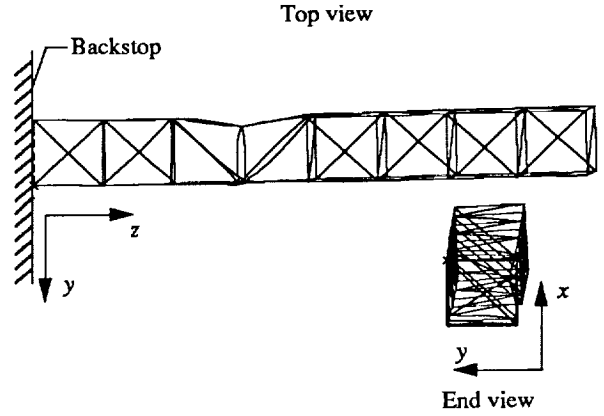

(b) Mode 2 at 5.76 Hz.

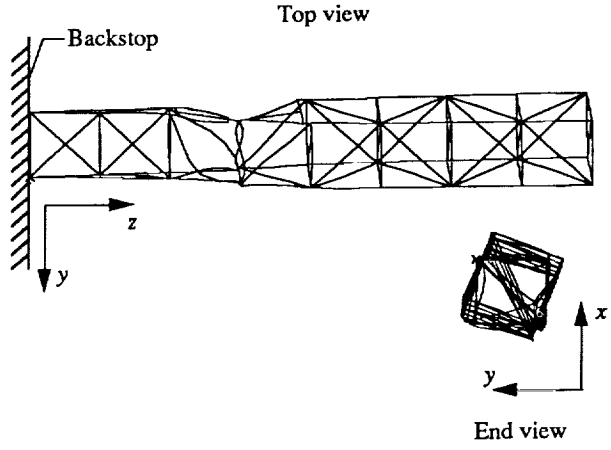

(c) Mode 3 at 15.34 Hz.

Figure 24. First three ATTB analytical mode shapes.

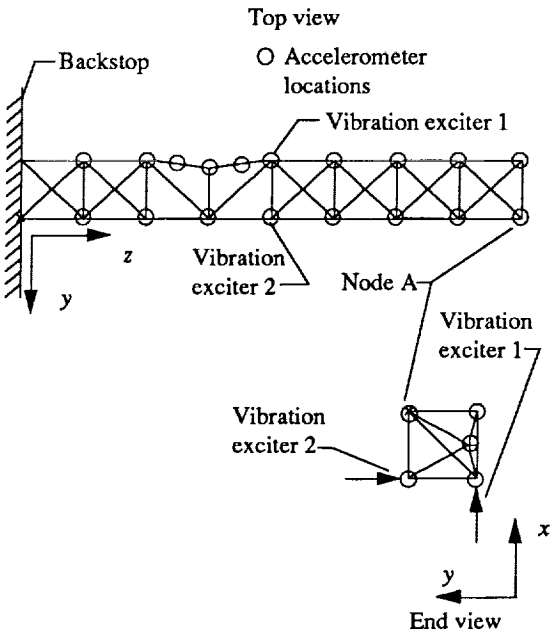

Figure 25. ATTB dynamic test configuration.

Experimental frequencies and mode shapes were calculated from the accelerometer data as before. In figure 26(a) the magnitude component of an experimental FRF is shown with three distinct peaks. This FRF corresponds to the x-response of node A at the ATTB free end (see fig. 25) because of the random forces applied in the x-direction by vibration exciter 1. The three peaks indicated three distinct modes with frequencies at 5.72, 15.29, and 24.05 Hz. These three frequencies corresponded to a first bending, a first torsion, and a second bending mode shape, respectively.

In figure 26(b), the magnitude component of a second experimental FRF is shown. This FRF corresponds to the y-response of node A due to the random forces applied by vibration exciter 2. The four peaks indicated four distinct modes with frequencies at 5.51, 15.29, 19.90, and 24.05 Hz. These four frequencies corresponded to a first bending, first torsion, and two second bending modes, respectively.

The two FRF's indicated that the first bending modes (5.51 and 5.72 Hz) were primarily characterized as bending about the x- and y-axes, respectively, because only one first bending mode was excited by random forces in either the x- or y-directions. This behavior of the first bending modes was predicted in the analytical mode shapes (see fig. 24) and was primarily attributed to the difference in stiffness properties between the two truss booms and the ATJ. The first three experimentally determined frequencies for the ATTB were 19, 18, and 38 percent less than the corresponding first three experimental frequencies of the RT. The first three analytical frequencies for the ATTB were 18, 18, and 37 percent less than the corresponding first three analytical frequencies of the RT. The correlation between the experimental and analytical frequency reductions between the RT and ATTB was within ±1 percent for the first three frequencies. This indicates that the relative performance is predictable between the RT and ATTB if linear and zero-backlash actuators are employed.

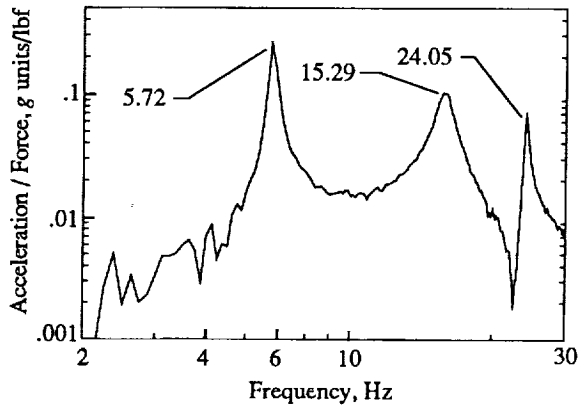

(a) x-response at node A due to vibration exciter 1.

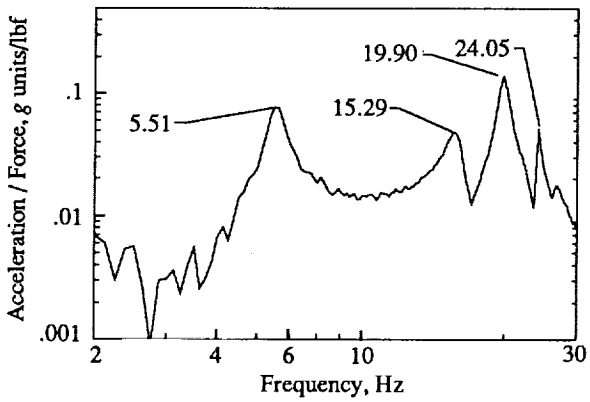

(b) y-response at node A due to vibration exciter 2.

Figure 26. Frequency response functions for ATTB.

In table 2 the first six analytical and experimental frequencies are listed along with the percent of difference in frequency between experiment and analysis, a mode shape description, and corresponding modal damping values. The first six experimental and analytical mode shapes were plotted and then individually compared to match mode shapes at the respective frequencies. The first five analytical mode shapes compared well with the first five experimental mode shapes determined from low-level excitation tests. The corresponding frequencies were within ±1 per-

cent for modes 1–3, within ±5 percent for mode 4, and within ±2 percent for mode 5. The sixth experimental frequency was within ±4 percent of the analytical frequency, and the mode shape was primarily characterized as a local mode of the ATJ. This mode shape did not compare well with the corresponding analytical mode shape, suggesting that further modal testing and analysis of the ATJ might be necessary to explain this mode. The fourth and sixth analytical mode shapes are shown in figures 27(a) and 27(b), respectively. These two mode shapes were selected for further analysis because of the difference between the respective analytical and experimental frequencies and to examine any lateral vibrations of the ATJ components at the higher frequencies.

The fourth and sixth analytical mode shapes were used to calculate the percent of strain energy due to bending deformations in the finite elements representing the ATJ. This calculation permits an assessment of the relative bending deformations occurring for a particular mode shape. For the fourth mode shape, 26 percent of the total strain energy was due to bending deformation in the ATJ components. For the sixth mode shape, 56 percent of the total strain energy was due to bending deformations in the ATJ components. This bending effect can be seen in the lateral vibrations of the A-frame and in the diagonals for mode 4 and mode 6, as shown in the enlarged views of figures 27(a) and 27(b), respectively. An examination of the A-frame double hinges shows that each one is stabilized by only a portion of the bending and torsional stiffness of one or two struts. As a result, these double hinges are susceptible to rotations due to A-frame bending induced by the lateral vibrations of the ATJ struts. Consequently, if higher vibration modes involving primarily lateral vibrations of the struts are of concern, their impact on double hinge stabilization should be carefully considered.

Table 2. Comparison of Analytical and Experimental Frequencies for the Articulated-Truss Test-Bed (ATTB)

Mode	Frequency, Hz		Difference, percent	Mode shape description	Modal damping, percent
	Analytical	Experimental			
1	5.52	5.51	−0.2	First bending	4.73
2	5.76	5.72	− .7	First bending	1.02
3	15.34	15.29	− .3	First torsion	3.89
4	18.90	19.90	5.0	Second bending	2.85
5	23.58	24.05	2.0	Second bending	.94
6	33.98	32.84	−3.5	Actuator shaft bending	2.05

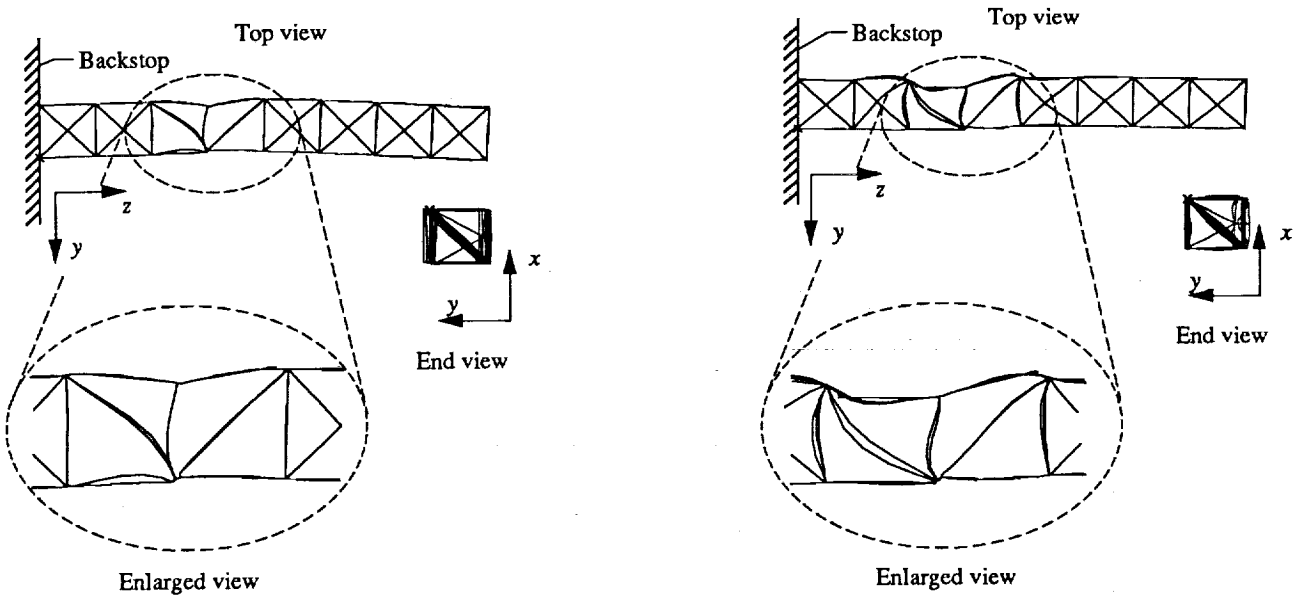

(a) Mode 4 at 18.90 Hz.

(b) Mode 6 at 33.98 Hz.

Figure 27. Fourth and sixth analytical mode shapes.

The sixth mode shape was considered primarily a local mode of the ATJ because of the large percentage of strain energy occurring in the ATJ components. Of the total strain energy, 23 percent was due to bending deformations in the actuators and their support beams for this mode. The high percentage of bending strain energy present in the actuators and support beams also suggests that the experimental bending characterization should be considered.

The first ATTB experimental mode had a modal damping value of 4.73 percent, followed by 3.89 percent for the first torsion mode (mode 3), and 2.85 percent for the first second bending mode (mode 4). These modal damping values were substantially greater than the largest modal damping value of the RT which was 0.78 percent. Whether the higher modal damping experienced in the ATTB was attributable to the hinges or to the actuators has not been determined.

Concluding Remarks

An articulated-truss space crane concept has been described, and structural characterization results have been presented for a first-generation space crane articulated-truss joint (ATJ). The ATJ was integrated into a structural test-bed referred to as the articulated-truss test-bed (ATTB). This test-bed was used to statically and dynamically characterize the ATJ in a configuration that approximated an operational environment. Load-deflection response and axial stiffness were also experimentally determined for one linear actuator of the ATJ. Static characterization was performed by applying known loads and measuring the corresponding deflections to obtain load-deflection curves. Dynamic characterization was performed using modal testing to experimentally determine the first six mode shapes, frequencies, and modal damping values. The static and dynamic characteristics were also determined for a reference truss (RT), which served as a characterization baseline for the ATTB static and dynamic tests. The first six analytical and experimental modes shapes were plotted and individually compared to verify matching modes at the respective frequencies. The RT and ATTB were assembled from truss hardware that was developed for the Precision Segmented Reflector (PSR) Technology Development Program. This truss hardware had been experimentally tested during the PSR Program to obtain bending and axial stiffness properties. Analytical predictions were obtained for the RT and ATTB static and dynamic characteristics from linear finite element analysis. The RT was also used to verify the predictability of the truss hardware based on the previously obtained experimental stiffness values.

The RT analytical predictions correlated well with the experimental results obtained from the static and dynamic characterization. For the static characterization, the RT load-deflection response was linear over the entire load range, and the experimental static characterization agreed within ± 1.0 percent of the analytical predictions. For the dynamic characterization, the first six experimental frequencies agreed within ± 1.7 percent of the corresponding analytical predictions. The RT modal damping values were determined to be less than 0.8 percent for the first six modes, which indicated that the RT hardware had very low structural damping. As evidenced by this correlation, good analytical predictions can be obtained for the RT by using the experimental stiffness values determined during the PSR program. Furthermore, the joint end hardware has been shown to exhibit a repeatable performance in that the hardware stiffness properties that were experimentally determined for the PSR Program were used to accurately predict the RT static and dynamic characteristics.

The ATTB load-deflection response was essentially linear but with some backlash in the region of low applied loading. The backlash was primarily due to the actuators in the ATJ, with a small amount due to the hinges. This emphasizes the importance of using higher fidelity actuators that have substantially reduced levels of backlash. The ATTB experimental load-deflection slope was approximately 261 lbf/in., and the corresponding analytical prediction was approximately 18 percent greater than this value. For the dynamic characterization, the experimental and analytical frequencies were within ± 1 percent for modes 1–3, within ± 5 percent for modes 4 and 6, and within ± 2 percent for mode 5. The ATTB exhibited significantly higher levels of modal damping than the RT, with a maximum modal damping value of 4.73 percent for the first mode. Whether the larger structural damping was primarily due to the actuators or to the hinges has not been determined. Bending deformations were noted in the ATJ components during the load-deflection testing and the corresponding finite element analysis. Lateral vibrations of the ATJ components also occurred with the higher vibration modes. This suggests that experimental bending characterization is also needed to accurately model the ATJ components. Further testing is also needed to determine the load-deflection characteristics of the single and double hinges. These test results will indicate the amount of backlash associated with the hinges and their stiffness properties.

The physical behavior observed during the experimental testing and analysis is currently being used to improve future ATJ designs. Some of the improvements include reducing load path eccentricities associated with double hinges by using single hinges where possible, and increasing the bending and torsional stiffness properties of the ATJ by increasing the ATJ strut stiffness properties, particularly for the struts comprising the ATJ A-frame.

NASA Langley Research Center
Hampton, VA 23665-5225
April 9, 1992

References

1. Cirillo, William M.; Troutman, Patrick A.; Brender, Karen D.; Dahlstrom, Eric L.; Ayers, J. Kirk; and Waters, Laura M.: Low Earth Orbit Infrastructure To Accommodate Manned Lunar Missions. *Engineering, Construction, and Operations in Space II: Volume 2,* Stewart W. Johnson and John P. Wetzel, eds., American Soc. of Civil Engineers, 1990, pp. 895–904.

2. Mikulas, Martin M., Jr.; and Dorsey, John T.: An Integrated In-Space Construction Facility for the 21st Century. *The 21st Century in Space, Volume 70 of Advances in the Astronautical Sciences,* George V. Butler, ed., American Astronautical Soc., 1990, pp. 75–92. (Available as AAS 88-167.)

3. Mikulas, M. M., Jr.; Davis, R. C.; and Greene, W. H.: *A Space Crane Concept: Preliminary Design and Static Analysis.* NASA TM-101498, 1988.

4. Gossain, D. M.; and Smith, P. J.: Structural Design and Test of the Shuttle RMS. *Environmental Effects on Materials for Space Applications,* AGARD-CP-327, Mar. 1983, pp. 2-1–2-10.

5. Graham, J. D.; Ravindran, R.; and Knapp, K.: Space Manipulators—Present Capability and Future Potential. *A Collection of Technical Papers - AIAA/NASA Conference on Advanced Technology for Future Space Systems,* American Inst. of Aeronautics and Astronautics, Inc., May 1979, pp. 243–253. (Available as AIAA Paper 79-0903.)

6. Gunkel, R. J.; Holmen, R. E.; and Tschirgi, J. M.: A Crane for Construction in Space. AIAA Paper 78-1666, Sept. 1978.

7. McCullough, J. R.: The Remote Manipulator System Second Generation Schemes. *Human Factors: Science for Working and Living—Proceedings of the Human Factors Society 24th Annual Meeting,* Human Factors Soc., 1980, pp. 209–213.

8. Sutter, Thomas R.; Bush, Harold G.; and Wallsom, Richard E.: An Articulated-Truss Space Crane Concept. *A Collection of Technical Papers, Part 4—AIAA/ASME/ASCE/AHS/ASC 31st Structures, Structural Dynamics and Materials Conference,* American Inst. of Aeronautics and Astronautics, Inc., Apr. 1990, pp. 2117–2125. (Available as AIAA-90-0994-CP.)

9. Watson, J. J.; Heard, W. L., Jr.; Bush, H. G.; Lake, M. S.; Jensen, J. K.; Wallsom, R. E.; and Phelps, J. E.: *Results of EVA/Mobile Transporter Space Station Truss Assembly Tests.* NASA TM-100661, 1988.

10. Bush, Harold G.; Herstrom, Catherine L.; Heard, Walter L., Jr.; Collins, Timothy J.; Fichter, W. B.; Wallsom, Richard E.; and Phelps, James E.: Design and Fabrication of an Erectable Truss for Precision Segmented Reflector Application. *A Collection of Technical Papers, Part 4 - AIAA/ASME/ASCE/AHS/ASC 31st Structures, Structural Dynamics and Materials Conference,* American Inst. of Aeronautics and Astronautics, Inc., Apr. 1990, pp. 454–462. (Available as AIAA-90-0999-CP.)

11. Whetstone, W. D.: *EISI-EAL Engineering Analysis Language User Instructions, Version 312.08.* Engineering Information Systems, Aug. 1985.

12. Clough, Ray W.; and Penzien, Joseph: *Dynamics of Structures.* McGraw-Hill, Inc., c.1975.

13. Timoshenko, S. P.; and Young, D. H.: *Theory of Structures, Second ed.* McGraw-Hill, Inc., c.1965.

14. *Computer-Aided Test System Operating Manual Software Version 3.0.* Doc. No. 2515-0100, Revision 4, GenRad, Inc., c.1988.

15. *I-DEAS Modal-Plus™ V10.0 Release Information.* P-0800, Structural Dynamics Research Corp., c.1991.

REPORT DOCUMENTATION PAGE

Form Approved
OMB No. 0704-0188

1. AGENCY USE ONLY *(Leave blank)*	2. REPORT DATE	3. REPORT TYPE AND DATES COVERED
	May 1992	Technical Memorandum

4. TITLE AND SUBTITLE
Structural Characterization of a First-Generation Articulated-Truss Joint for Space Crane Application

5. FUNDING NUMBERS
WU 506-43-41-02

6. AUTHOR(S)
Thomas R. Sutter, K. Chauncey Wu, Kevin T. Riutort, Joseph B. Laufer, and James E. Phelps

7. PERFORMING ORGANIZATION NAME(S) AND ADDRESS(ES)
NASA Langley Research Center
Hampton, VA 23665-5225

8. PERFORMING ORGANIZATION REPORT NUMBER
L-17061

9. SPONSORING/MONITORING AGENCY NAME(S) AND ADDRESS(ES)
National Aeronautics and Space Administration
Washington, DC 20546-0001

10. SPONSORING/MONITORING AGENCY REPORT NUMBER
NASA TM-4371

11. SUPPLEMENTARY NOTES
Sutter, Wu, and Riutort: Langley Research Center, Hampton, VA; Laufer and Phelps: Lockheed Engineering & Sciences Company, Hampton, VA.

12a. DISTRIBUTION/AVAILABILITY STATEMENT
Unclassified–Unlimited

Subject Category 18

12b. DISTRIBUTION CODE

13. ABSTRACT *(Maximum 200 words)*

A first-generation space crane articulated-truss joint was statically and dynamically characterized in a configuration that approximated an operational environment. The articulated-truss joint was integrated into a test-bed for structural characterization. Static characterization was performed by applying known loads and measuring the corresponding deflections to obtain load-deflection curves. Dynamic characterization was performed using modal testing to experimentally determine the first six mode shapes, frequencies, and modal damping values. Static and dynamic characteristics were also determined for a reference truss that served as a characterization baseline. Load-deflection curves and experimental frequency response functions are presented for the reference truss and the articulated-truss joint mounted in the test-bed. The static and dynamic experimental results are compared with analytical predictions obtained from finite element analyses. Load-deflection response is also presented for one of the linear actuators used in the articulated-truss joint. Finally, an assessment is presented for the predictability of the truss hardware used in the reference truss and articulated-truss joint based upon hardware stiffness properties that were previously obtained during the Precision Segmented Reflector (PSR) Technology Development Program.

14. SUBJECT TERMS	15. NUMBER OF PAGES
Space crane; In-space assembly; Experimental testing; Articulated-truss joints; Static analysis; Normal modes analysis	22
	16. PRICE CODE A03

17. SECURITY CLASSIFICATION OF REPORT	18. SECURITY CLASSIFICATION OF THIS PAGE	19. SECURITY CLASSIFICATION OF ABSTRACT	20. LIMITATION OF ABSTRACT
Unclassified	Unclassified		